J Nanopart Res (2018) 20: 38
https://doi.org/10.1007/s11051-018-4143-4

RESEARCH PAPER

A facile in situ solvothermal method for two-dimensional layered g-C_3N_4/SnS_2 p-n heterojunction composites with efficient visible-light photocatalytic activity

Juan Feng · Ji-bing Chen · Jiang-long Mu · Li-da Chen · Hui Miao · En-zhou Liu · Jun Fan · Xiao-yun Hu

Received: 26 October 2017 / Accepted: 19 January 2018 / Published online: 6 February 2018

Abstract To overcome the fast recombination rate of electron-hole pairs of individual SnS_2, p-n heterojunction g-C_3N_4/SnS_2 composites were fabricated as high-efficiency visible-light photocatalyst to photodegradate the organic dye MB. The morphologies, structures, compositions, and photocatalytic properties were characterized. The SnS_2 shows two-dimensional layer structure with an average thickness of 20 nm and diameter size of about 2 μm, and the g-C_3N_4 nanoflakes were uniformly deposited on the surface of SnS_2 nanosheets. In comparison with the bare g-C_3N_4 and SnS_2, the composites show improved photocatalytic activity under visible light, which is sensitive to the content of g-C_3N_4. In particular, the 15% g-C_3N_4/SnS_2 composites exhibit the highest photocatalytic activity and outstanding reusability, which can degrade 88.01% MB after only 1 h in the visible light ($\lambda > 420$ nm) range. The g-C_3N_4/SnS_2 heterojunction composites show outstanding reusability after four times cycling experiments. The improved photocatalytic activities of composites are attributed to abundant active species, increased charge separation, and decreased electron-hole pair recombination, which originated from the large specific surface area and efficient interfacial transport of photo-induced charge carriers between SnS_2 and g-C_3N_4. These results suggest that the two-dimensional layered g-C_3N_4/SnS_2 p-n heterojunction composites are promised to be a high-efficiency visible-light photocatalyst.

Keywords p-n heterojunction · g-C_3N_4/SnS_2 · Synergistic effect · Photocatalyst

J. Feng · J.-l. Mu · L.-d. Chen · H. Miao · X.-y. Hu (✉)
School of Physics, Northwest University, Xi'an 710069, China
e-mail: hxy3275@nwu.edu.cn

J.-b. Chen · E.-z. Liu · J. Fan
School of Chemical Engineering, Northwest University, Xi'an 710069, China

E.-z. Liu
Institute of Modern Physics, Northwest University, Xi'an 710069, China

Introduction

Environmental problems relating to the organic pollutant in water were becoming an increasingly serious issue for human health in modern society. Prussian blue (MB, Fe_4 [Fe $(CN)_6]_3$), as a common pigment, has been widely used in the daily life and printing industry. However, the high biotoxicity and nonbiodegradable characteristic make it urgently needed to avoid water pollution (Baghriche et al. 2017). Nowadays, enormous works have been paid to remove the contaminants from water, for example, filtration, physical adsorption, chemical oxidation, biodegradation, and so on (Ganjalinia et al. 2017). Among them, photocatalytic degradation has attracted much attention, due to its efficient and environmental-friendly characteristics (Yuan et al. 2015; Shao et al. 2014). TiO_2 have been widely used as commercial photocatalysts, owing to its low cost, easy fabrication, chemical stability, and nontoxicity (Marien et al. 2016; Ivanova et al. 2016). However,

the photocatalytic activity of TiO_2 can only perform in the ultraviolet light owing to its wide band gap, greatly limiting its applications (Zhou et al. 2017). Therefore, the exploration of novel visible-light response photocatalysts has drawn ever-increasing interest (Wu et al. 2017).

As a typical n-type semiconductor, tin sulfides (SnS_2) has been considered to be a visible-light-response photocatalysts due to its narrow indirect band gap of ~ 2 eV (Li et al. 2016; Li et al. 2012; Zhang et al. 2017; Zhang et al. 2010). Besides, SnS_2 has a layered hexagonal CdI_2-type crystal structure, which is easily fabricated into two-dimensional (2D) layered nanostructures (Ren et al. 2016). The large specific surface area of 2D layered SnS_2 nanosheets has plentiful active site, leading to superior charge transport ability (Zhang et al. 2015a, b; Bian et al. 2013). However, the electron-hole pair recombination rate of SnS_2 is fast, restricting its photocatalytic abilities. To solve this problem, decorating n-type SnS_2 nanosheets with an appropriate p-type semiconductor, which can generate new interfacial charge channels and facilitate the separation of photoelectrons from vacancies, is believed to be significant to enhance the photocatalytic capability of SnS_2. g-C_3N_4, as a representative p-type semiconductor, has drawn considerable interests owing to the special layer structure, strong visible-light absorption, and optical performances (Liu et al. 2016; Cao et al. 2015; Wang et al. 2012; Miao et al. 2017; Wang et al. 2009; Pu et al. 2017; Ramadan et al. 2013). Several works have reported that the g-C_3N_4/SnS_2 heterojunction shows excellent photocatalytic activity under visible light in the photodegradation of MO, RhB, Cr^{6+}, and so on (Chen et al. 2016; Deng et al. 2017; Di et al. 2017; Sun et al. 2014; Zhang et al. 2015b). Bin Dong group presents the 2D/2D SnS_2 and g-C_3N_4 nanosheets heterojunction photocatalysts through ultrasonic dispersion method. However, the fabrication method is tedious and takes too much time (Zhang et al. 2015b). Moreover, Jimin Xie team has proposed SnS_2/g-C_3N_4 composite by a wet precipitation method, but the MO degradation over the photocatalyst is only 53.02% after 1 h (Chen et al. 2016). In our best knowledge, no paper has been reported the usage of g-C_3N_4/SnS_2 heterojunction to photodegradate MB in visible light. Moreover, uniformly coupling SnS_2 nanosheets with g-C_3N_4 nanoflakes, which can provide sufficient charge channels and active sites, is still a big challenge.

In this work, a novel p-n heterojunction g-C_3N_4/SnS_2 photocatalyst was prepared via a facile solvothermal route for the photodegradation of MB. The g-C_3N_4/SnS_2 photocatalyst have a large surface area and can accelerate the separation of electron-hole pairs, leading to improved photocatalytic performance compared to the bare SnS_2 and g-C_3N_4. A possible enhancement mechanism for the p-n heterojunction g-C_3N_4/SnS_2 photocatalyst was proposed.

Experimental

Preparation of 2D layered g-C_3N_4/SnS_2 composites

The bulk g-C_3N_4 was fabricated via a thermal polymerization route (Zhao et al. 2014; Ma et al. 2015). Melamine (10 g) was annealed at 550 °C with a heating speed of 5 °C per minute and maintained for 4 h in a muffle furnace and in the air. The obtained yellow products were collected and ground into powders. Then, under ultrasound treatment, an appropriate content of the obtained g-C_3N_4 powders was dispersed into 60 ml ethanol solution containing 0.7 g $SnCl_4{\cdot}5H_2O$. After that, 0.75 g of thioacetamide was added and magnetically stirred for 5 h. Finally, the obtained solution was added into a 100-ml capacity of autoclave, which was heated at 180 °C for 12 h. By washing with deionized water and ethanol, the products were obtained. The g-C_3N_4/SnS_2 composite containing 5, 10, 15, 20, and 30 wt% of g-C_3N_4 was fabricated and named as SSCN-5, SSCN-10, SSCN-15, SSCN-20, SSCN-30, respectively. Besides, pure SnS_2 was fabricated through a similar procedure in the absence of g-C_3N_4.

Characterizations

The products were characterized by X-ray diffraction instrument (XRD, DX-2700, Cu Kα radiation, $\lambda = 1.5406$ Å), scanning electron microscope (SEM, JSM-6390A), transmission electron microscope (TEM, FEI Tecnai G^2 F20), X-ray photoelectron spectroscopy (XPS, ESCALAB210), UV-visible spectrophotometer (UV-3600, Shimadzu), N_2 adsorption-desorption isotherms (Quantachrome NOVA 2000e), and elemental analysis (EA, vario MACRO cube).

Photocatalytic experiments

The photocatalytic performance was assessed by photodegradatin of MB dye solution. A 300 W Xe lamp with a cut-off filter of 420 nm was served as the visible light source. Fifty milligrams of samples was added into a 50 ml water solution containing 20 mg/L MB. Three milliliter of solution was collected and centrifuged at defined time intervals, and then the MB content was measured. All the experiments were operated at room temperature in air.

Photocurrent measurements

Photocurrent experiment was performed by an electrochemical workstation (CHI 660E, China), using a standard three-electrode system and 0.5 mol/L of Na_2SO_4 as electrolyte. The photoelectric currents were measured by a 150 W Xe lamp.

The working electrode was prepared as follows (Mu et al. 2017): first, fluorine-doped tin oxide (FTO) glass substrates with a size of 2.0 × 1.0 cm were cleaned with acetone, ethanol, and deionized water under ultrasonic treatment for 30 min and dried in a vacuum oven. Second, 5 mg of the as-prepared sample was dissolved in 1 ml of acetone with ultrasonic dispersion for 2 h. After that, the dispersed sample solution was uniformly dropped onto the FTO conductive surface until it dried naturally. Third, the photoelectrode was heated to 200 °C for 2 h at 2 °C/min. Finally, the photoelectrode was cooled to room temperature and then collected for testing.

Results and discussions

Figure 1 shows the XRD patterns of bare SnS_2, g-C_3N_4, and g-C_3N_4/SnS_2 heterojunction composites. All the diffraction peaks of pure SnS_2 (Fig. 1a) suggest the formation of SnS_2 with hexagonal phase, which is accordant with the JCPDS card of 23-0677. No other diffraction peaks of impurity were detected. The XRD pattern of bare g-C_3N_4 (Fig. 1g) shows two diffraction peaks at 13.02°, 27.87°, which is attributed to the (100) and (002) crystal planes of g-C_3N_4 with JCPDS card of 87-1526. All the diffraction peaks of g-C_3N_4/SnS_2 heterojunction composite (Fig. 1b–f) are accordant with SnS_2 and g-C_3N_4. The elemental analysis results show that the actual weight of g-C_3N_4 in SSCN-5, SSCN-10, SSCN-15, SSCN-20, and SSCN-30 are 2.78, 7.64, 11.86, 15.69, and 23.09%, respectively.

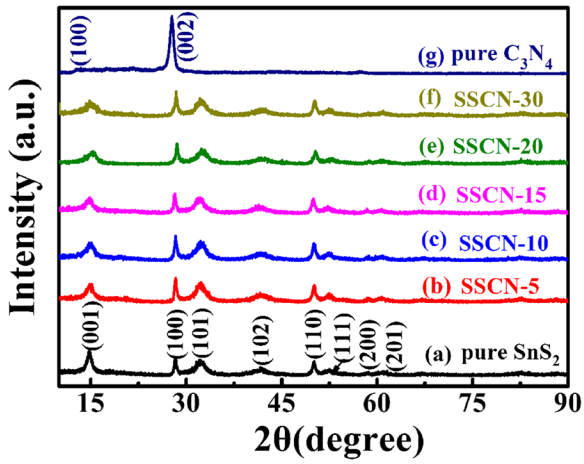

Fig. 1 XRD patterns of SnS_2, g-C_3N_4 and g-C_3N_4/SnS_2 composites

Figure 2a shows a representative morphology of SnS_2, which is two-dimensional layer larger sheets structure with average thickness of 20 nm and average diameter size of about 2 μm, and the surfaces were relatively smooth. The g-C_3N_4 (Fig. 2b) exhibits flake-like nanostructure. Figure 2c–g reveals the SEM images of g-C_3N_4/SnS_2 nanocomposites with different g-C_3N_4 contents. Obviously, the SnS_2 in the nanocomposites still remain sheet structure, indicating that the addition of g-C_3N_4 has little influence on the growth of SnS_2 nanosheets. EDS spectrum of g-C_3N_4/SnS_2 catalyst (Fig. 2h) contains Sn, S, C, and N elements. The chemical element distributions of composites were further studied using elemental mapping analysis techniques, as shown in Fig. 2i–l. It is clear that the C and N elements are throughout the SnS_2 nanosheets and g-C_3N_4 was successfully combined with SnS_2.

Figure 3a shows a typical TEM image of the pure SnS_2. The pure SnS_2 shows a flower-like shape, which are assembled by thin nanosheets. HRTEM image of pure SnS_2 (Fig. 3b) shows that the interplanar distance is 0.316 nm, which can be assigned to the (100) crystallographic plane of hexagonal SnS_2. The selected area electron diffraction (SAED) of a single nanosheet of pure SnS_2 (Fig. 3c) shows several dot lattices, indicating the single crystalline nanostructure of single SnS_2 nanosheets. TEM image of g-C_3N_4 (Fig. 3d) reveals a thin and irregular nanoflakes structure. Figure 3e shows TEM images of g-C_3N_4/SnS_2 nanocomposites. The magnification images of the local area A and B marked

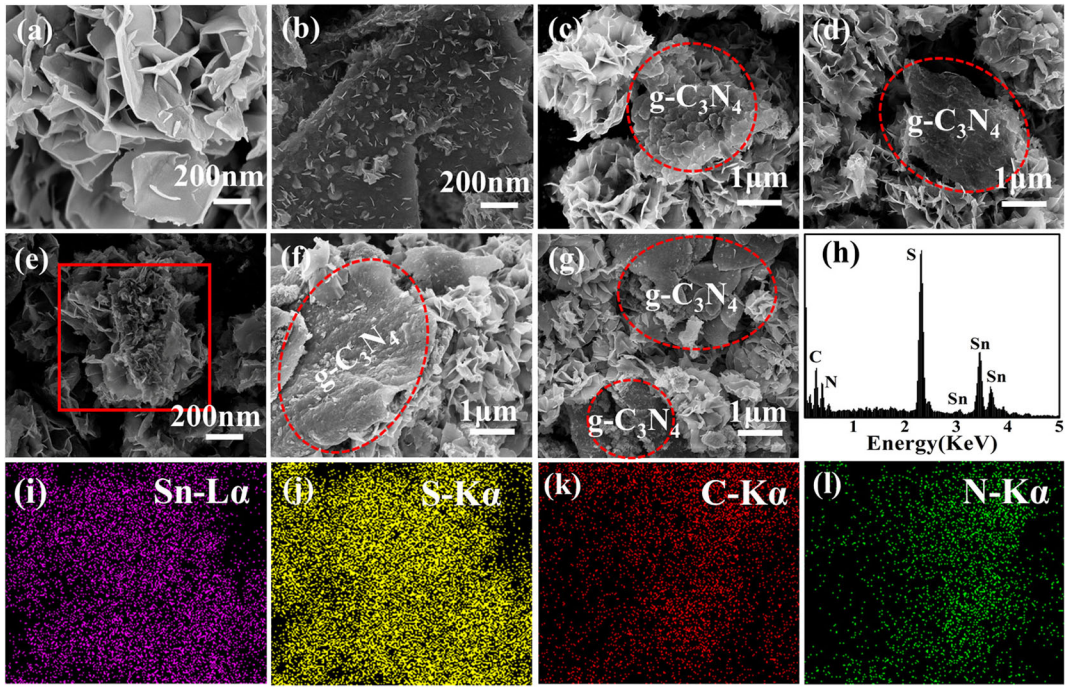

Fig. 2 SEM images of **a** SnS_2, **b** g-C_3N_4, **c** SSCN-5, **d** SSCN-10, **e** SSCN-15, **f** SSCN-20, and **g** SSCN-30. **h** EDS spectrum of SSCN-15. Elemental mapping images of **i** Sn, **j** S, **k** C, and **l** N elments

by white box in (e) are shown in Fig. 3f, g. Obviously, the g-C_3N_4 nanoflakes are uniformly decorated on the surface of SnS_2 nanosheets, suggesting the formation of g-C_3N_4/SnS_2 heterojunction structure. Figure 3h shows the HRTEM mages of the area C marked by white circle in (f), and Fig. 3i shows the HRTEM mages of the area D marked by white circle in (g). HRTEM image of SnS_2 in g-C_3N_4/SnS_2 nanocomposites shows an interplanar distance of 0.312 nm, which is accordant with the (100) plane of SnS_2. While HRTEM image of g-C_3N_4 nanoplates in the nanocomposites does not show obvious lattice.

Figure 4a reveals the UV-vis absorption spectra of SnS_2, g-C_3N_4, and g-C_3N_4/SnS_2 heterojunction composites. The optics absorption of g-C_3N_4/SnS_2 composites slightly move to red range by increasing the amount of g-C_3N_4. The band gap energy (E_g) can be obtained by the equation as follows:

$$(\alpha h\nu) = A\left(h\nu - E_g\right)^{n/2} \quad (1)$$

where α is the efficiency of light absorption, A is constant, h is frequency of light, ν is photonic energy, E_g is energy of band gap, and n is a constant which is determined by the optical transition types of semiconductor. As a direct allowed transition semiconductor, the value of n for SnS_2 is 1. While for g-C_3N_4, n is equal to 4, since g-C_3N_4 is a kind of indirect allowed transition semiconductor. The E_g of SnS_2 and g-C_3N_4 have a gap value of about 2.14 and 2.76 eV, respectively. Obviously, the values of E_g for the g-C_3N_4/SnS_2 composites located between SnS_2 and g-C_3N_4, which becomes larger by increasing the amount of g-C_3N_4. The g-C_3N_4/SnS_2 composites exhibit a broader absorption range, which almost covers the whole visible light range.

XPS is commonly used to evaluate the surface chemical components and elemental valence states of materials. The survey scan XPS spectra of SSCN-15 composites (Fig. 5a) show several characteristic peaks related to the Sn 3d, S 2p, C 1s, and N 1s, confirming the existence of Sn, S, C, and N in the sample. The Sn 3d XPS spectrum of Fig. 5b shows two peaks at about 486.4 and 494.8 eV, corresponding to Sn $3d_{5/2}$ and Sn $3d_{3/2}$, respectively, which indicates that Sn is quadrivalent. No obvious Sn^{2+} peak (binding energy at about 485.8 eV) was detected in the Sn spectrum. High resolution XPS spectrum of S 2p (Fig. 5c) can be calculated into two peaks located at about 161.9 and 163.1 eV, which are associated to S $3p_{3/2}$ and S $3p_{1/2}$, respectively. Interestingly, in comparison with the pure SnS_2, the

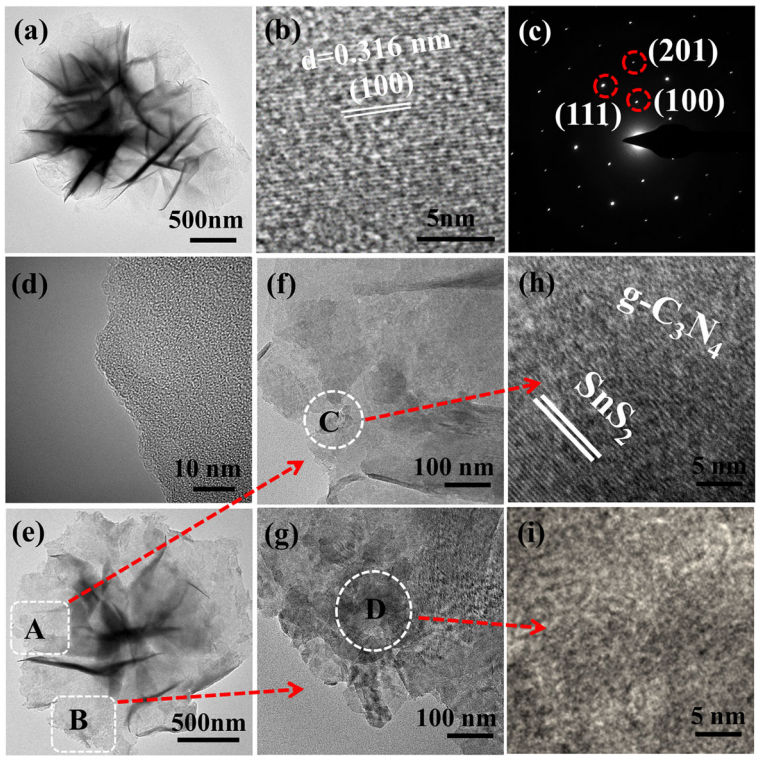

Fig. 3 **a** TEM image, **b** HRTEM image, and **c** SAED pattern of pure SnS_2. **d** TEM image of pure g-C_3N_4. **e** TEM image of g-C_3N_4/SnS_2 composite. **f** TEM images of the area A marked by white square in (**e**). **g** TEM images of the area B marked by white square in (**e**). **h** HRTEM mages of the area C marked by white circle in (**f**). **i** HRTEM mages of the area D marked by white circle in (**g**)

XPS peaks of Sn 3d and S 2p in g-C_3N_4/SnS_2 composite shift to lower binding energy ranges, which is probably due to the formation of interactions in the interface of g-C_3N_4/SnS_2 heterojunction composite (Mu et al. 2017). High resolution C1s spectrum (Fig. 5d) has two calculated peaks located at 284.5 and 288.5 eV, which is related to the C-C and N-C=N functional groups, respectively. High resolution N 1s spectrum (Fig. 5e) can be fitted by three peaks at 398.8, 399.5 and 401.1 eV, corresponding to the C-N=C, C-N-C and N-H functional groups, respectively (Hou et al. 2013; Ye et al. 2013; Chen et al. 2015).

Since surface area is a crucial factor of photocatalytic reduction rate, the specific surface areas of SnS_2, g-C_3N_4 and g-C_3N_4/SnS_2 composites were analyzed by nitrogen adsorption-desorption isotherms (BET), as shown in Fig. 6. The corresponding parameters are listed in Table 1. Obviously, the pure SnS_2 and g-C_3N_4 have a surface area of 10.12 and 29.89m^2/g, respectively. For the g-C_3N_4/SnS_2 composites, the surface areas are greatly increased by increasing the content of g-C_3N_4 from 5 to 15%, and then decreases by further increasing the g-C_3N_4 content from 15 to 30%. Among all the g-C_3N_4/SnS_2 composites, SSCN-15 has the largest BET surface area and displays a type-IV isotherm. The larger surface area is beneficial for the catalyst applications.

Figure 7a displays the photodegradation curves of SnS_2, g-C_3N_4 and g-C_3N_4/SnS_2 composites by degrading 20 mg/L MB solution. The comparison of corresponding photocatalytic degradation efficiencies for different catalysts after 1 h is displayed in Fig. 7b. It is clearly seen that the g-C_3N_4/SnS_2 composites show greatly enhanced synergetic photocatalytic activities compared to SnS_2 and g-C_3N_4. Besides, the photocatalytic activities of g-C_3N_4/SnS_2 composites are sensitive to the concentration of g-C_3N_4, which increase first and then decrease by increasing the amount of g-C_3N_4. The 15 wt% g-C_3N_4/SnS_2 (CNSS-15) composites show the highest photocatalytic activity, which can degrade 88.01% of MB after only 1 h under visible-light ($\lambda >$ 420 nm) irradiation. These results are possibly due to that moderate amount of g-C_3N_4 may induce abundant heterojunction interfaces in the g-C_3N_4/SnS_2 composites, which is fascinating for the separation of photo-induced electrons and holes, resulting in optical photocatalytic capacity. While continuously increasing the amount of g-C_3N_4 may result in the aggregation of g-C_3N_4 on the surface of SnS_2 nanosheets, which may

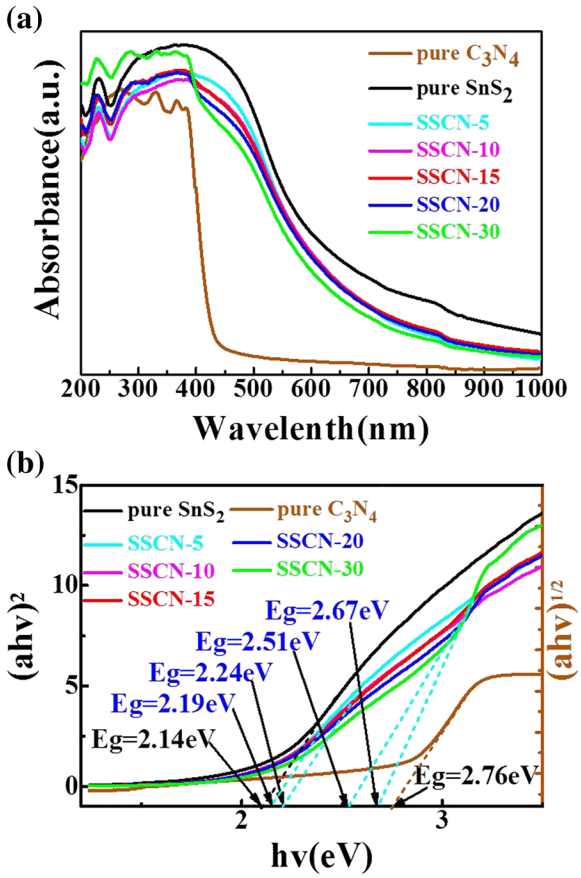

Fig. 4 **a** UV-vis absorption spectra of different samples, **b** Plot of $(\alpha h\nu)^2$ versus energy ($h\nu$) for the band gap of SnS_2 and g-C_3N_4/SnS_2 composites, and the plot of $(\alpha h\nu)^{1/2}$ versus energy ($h\nu$) for the band gap of pure g-C_3N_4

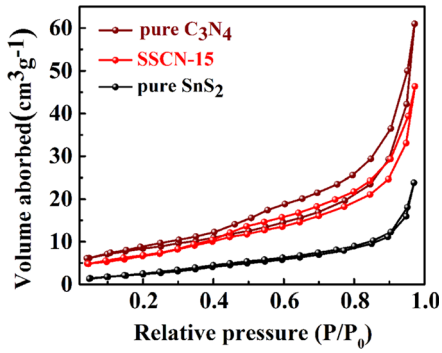

Fig. 6 BET curves of SnS_2, g-C_3N_4, and g-C_3N_4/SnS_2 composites

reduce the active sites and promote the recombination of electrons and holes.

The reaction kinetics of MB degradation for the catalysts is displayed in Fig. 7c, which are calculated by the pseudo first-order equation function mode (Chen et al. 2015):

$$-\ln(C_t/C_0) = k \cdot t \quad (2)$$

where k is the constant of pseudo-first-order rate (min^{-1}) and t is the irradiation time. Comparisons of k values of different samples are shown in Fig. 7d. Obviously, the optimal g-C_3N_4/SnS_2 composite (SSCN-15) show the highest k value of 0.0403 min^{-1}, which is about 3.3 and 7.9 times larger than that of pure SnS_2 (0.0103 min^{-1}) and g-C_3N_4 (0.0054 min^{-1}), respectively.

Recycling experiments of optimal SSCN-15 was further adopted to investigate the photocatalytic stability of g-C_3N_4/SnS_2 heterojunction composites, as presented in

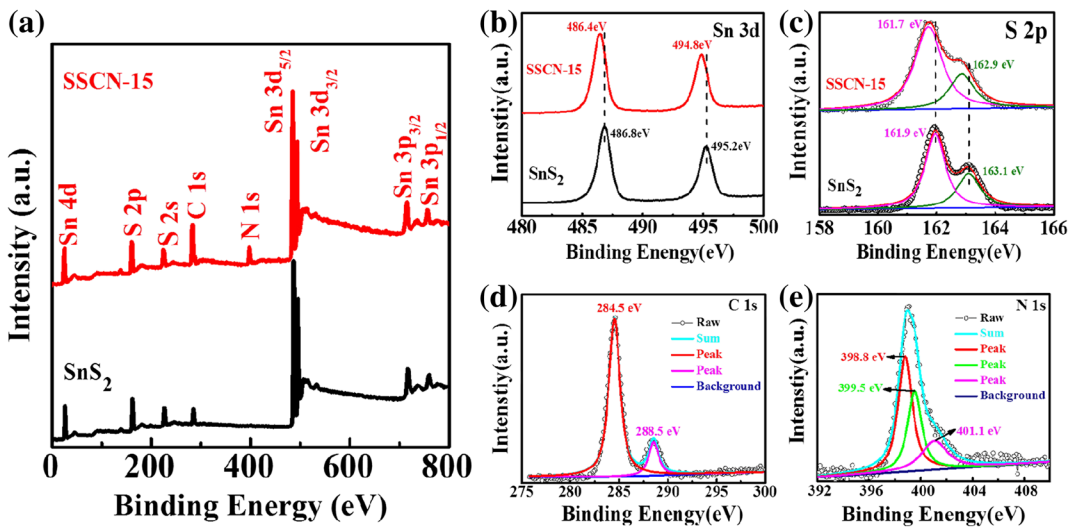

Fig. 5 XPS spectra: **a** survey scan of SnS_2 and g-C_3N_4/SnS_2 composites (SSCN-15). **b** Sn 3d spectrum, **c** S 2p spectrum, **d** C 1s spectrum, and **e** N 1s spectrum

Table 1 Physical properties of pure SnS_2, g-C_3N_4, and g-C_3N_4/SnS_2 composites

Samples	S_{BET} (m^2 g^{-1})	Pore volume (cm^3 g^{-1})	Pore diameter (nm)	Average pore size (nm)
SnS_2	10.12	0.04	6.99	12.84
SSCN-5	20.02	0.05	3.79	11.31
SSCN-10	25.47	0.07	3.82	11.59
SSCN-15	25.79	0.07	3.37	11.12
SSCN-20	25.48	0.07	3.80	12.23
SSCN-30	21.74	0.07	3.38	15.10
C_3N_4	29.89	0.08	3.40	12.62

Fig. 8a. Obviously, the rate of degradation remains larger than 80% even after four recycles under visible-light irradiation, which suggests that the catalyst has outstanding reusability. The XRD patterns of SSCN-15 before and after four recycling experiments (Fig. 8b) reveal that the crystal structure is not changed and the peak positions are nearly the same four recycling experiments, revealing that the optimal g-C_3N_4/SnS_2 composite has a good stability during the photocatalytic degradation process.

During the photocatalytic process, the photo-induced electron (e^-) and holes (h^+) can be further converted into other species, for example, superoxide radical ($\cdot O_2^-$) and hydroxyl radical (·OH). To investigate the effect of reactive species during the photodegradation process, h^+, $\cdot O_2^-$, and ·OH were trapped by ammonium oxalate

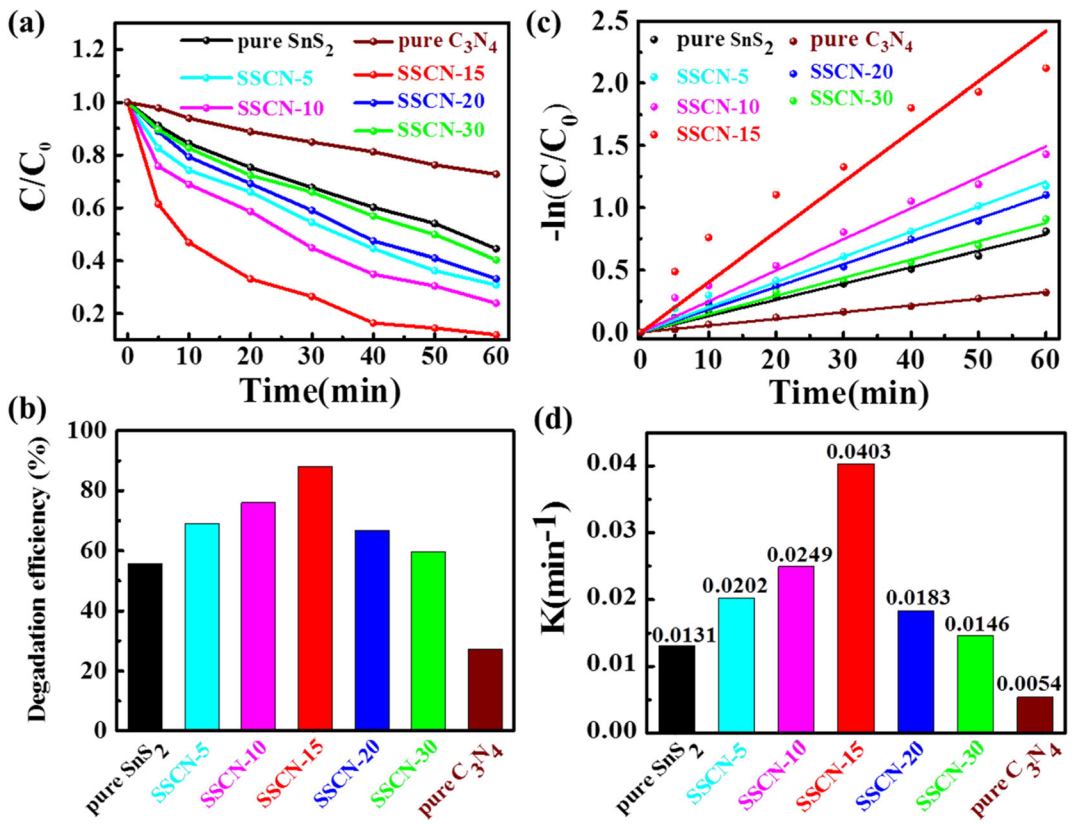

Fig. 7 **a** Photocatalytic degradation curves of MB using SnS_2, g-C_3N_4, and g-C_3N_4/SnS_2 composites as the photocatalyts in the visible light range. **b** The comparison of degradation efficiencies for different catalysts after 1 h. **c** The kinetic curves of different photocatalyts. **d** The rate constants of different photocatalyts

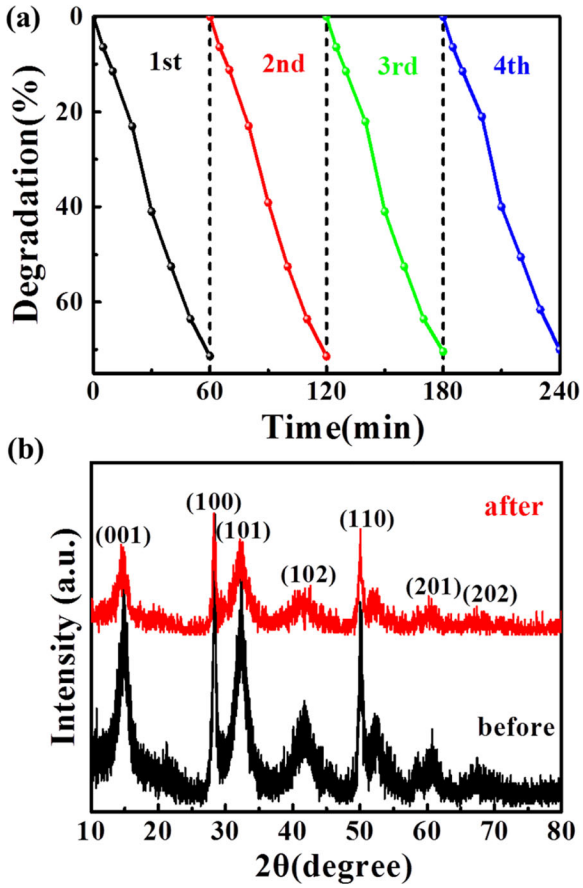

Fig. 8 **a** Cycling performance of g-C_3N_4/SnS_2 composites (SSCN-15) for photodegradation of MB. **b** XRD patterns of SSCN-15 before and after four recycling experiments under visible-light irradiation

(AO), benzoquinone (BQ), and isopropanol (IPA), respectively. The trapping experiments were the same as the MB photocatalytic degradation process. Before the degradation, scavengers were added into the solution. We can see that the degradation efficiency of MB is 88.01% without any scavenger (NS) from Fig. 9. When

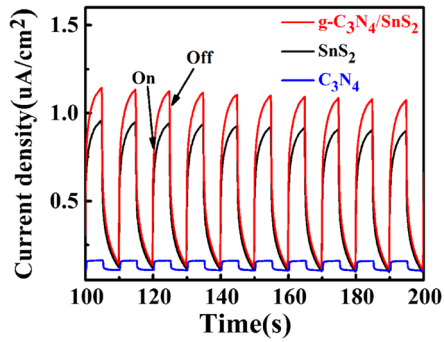

Fig. 10 Transient photocurrent curves of SnS_2, g-C_3N_4, and g-C_3N_4/SnS_2 composites (SSCN-15)

the scavengers were added, the degradation rate showed some changes. For instance, when AO was used, the rate of degradation is almost invariant. When IPA and BQ were introduced, the rates of degradation fall to 15.88 and 29.63%, respectively. Obviously, the main active species was ·OH during the degradation of MB.

Figure 10 reveals the photocurrent-time change curves of SnS_2, g-C_3N_4, and g-C_3N_4/SnS_2 (SSCN-15) composites. When the light is turned on, the photocurrent density rises quickly. And when the light is switch off, the photocurrent decrease at once. It can be seen that the photocurrent value of SSCN-15 composite is much higher than the pure SnS_2 and g-C_3N_4. This result reveals that the composite has the best separation efficiency and migration of electron-hole. This may explain why SSCN-15 composite exhibited the best photocatalytic activity compare with other samples (see Fig. 7a).

According to the band gap structure of photocatalysts and the effects of scavengers, an enhanced photocatalytic mechanism of the g-C_3N_4/SnS_2 heterojunction was proposed (Fig. 11). Using the irradiation of visible light, SnS_2 and g-C_3N_4 could be excited to generate some electron-hole pairs. When e^- was leaped into the conduction band, it leaved behind h^+ in the valence band.

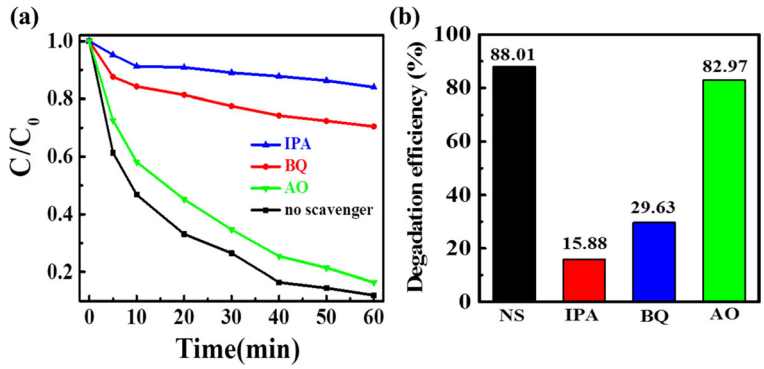

Fig. 9 Photodegradation of MB by g-C_3N_4/SnS_2 composites (SSCN-15) with different scavengers

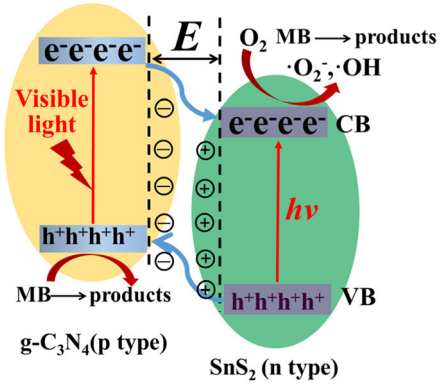

Fig. 11 Photocatalytic mechanism of the p-n heterojunction g-C_3N_4/SnS_2 photocatalyst for the degradation of MB over

The e^- and h^+ in g-C_3N_4 can inject into SnS_2. At the same time, p-n heterojunction was formed over the p-type g-C_3N_4 and n-type SnS_2 photocatalysts (Sun et al. 2014). The photo-induced electrons move from n-type SnS_2 to p-type g-C_3N_4 while the holes transfer from g-C_3N_4 to SnS_2, until the system got an equilibration of Fermi level. Then, an inner electron field (*E*) was created at the interface between g-C_3N_4 and SnS_2, resulting the effective separation of photo-induced electron and hole pairs. The photo-induced electrons further formed $\cdot O_2^-$ and ·OH species. Finally, all the active species reacted with MB solution. The p-n heterojunction g-C_3N_4/SnS_2 photocatalysts have exhibited better photocatalytic performance than pure SnS_2 and g-C_3N_4.

Conclusion

In summary, a novel p-n heterojunction g-C_3N_4/SnS_2 photocatalysts were fabricated via an in-situ solvothermal method for photodegradation of MB in the visible light range. The g-C_3N_4/SnS_2 heterojunction composites show improved photocatalytic capacities compared to SnS_2 and g-C_3N_4. The optimal composites show a high photodegradation efficiency of 88.01% after only 1 h and good reusability after 4 cycles. Then remarkable improved photocatalytic properties are associated to the abundant active species in the interfaces, sufficient separation of electrons and holes pairs, and improved charge transfer channels between the p-n heterojunction interfaces. This study demonstrated that the p-n g-C_3N_4/SnS_2 heterojunction composites are promised to be a novel synergetic visible-light-responsive photocatalyst.

Acknowledgements This work was supported by the National Natural Science Foundation of China (Nos. 51372201, 21476183, 21676213).

Compliance with ethical standards

Conflict of interest The authors declare that they have no conflict of interest.

References

Baghriche O, Rtimi S, Pulgarin C, Kiwi J (2017) Polystyrene CuO/Cu_2O uniform films inducing MB-degradation under sunlight. Catal Today 284:77–83. https://doi.org/10.1016/j.cattod.2016.10.018

Bian X, Lu X, Xue Y, Zhang C, Kong L, Wang C (2013) A facile one-pot hydrothermal method to produce SnS_2/reduced graphene oxide with flake-on-sheet structures and their application in the removal of dyes from aqueous solution. J Colloid Interface Sci 406:37–43. https://doi.org/10.1016/j.jcis.2013.05.075

Cao S, Low J, Yu J, Jaroniec M (2015) Polymeric photocatalysts based on graphitic carbon nitride. Adv Mater 27(13):2150–2176. https://doi.org/10.1002/adma.201500033

Chen L, Chen M, Jiang D, Xie J (2016) A facile strategy for SnS_2/g-C_3N_4 heterojunction composite and the mechanism in photocatalytic degradation of MO. J Mol Catal A Chem 425:174–182. https://doi.org/10.1016/j.molcata.2016.10.003

Chen X, Zhou B, Yang S, Wu H, Wu Y, Wu L, Pan J, Xiong X (2015) In situ construction of an SnO_2/g-C_3N_4 heterojunction for enhanced visible-light photocatalytic activity. RSC Adv 5(84):68953–68963. https://doi.org/10.1039/C5RA11801H

Deng F, Zhao LN, Pei XL, Luo XB, Luo SL (2017) Facile in situ hydrothermal synthesis of g-C_3N_4/SnS_2 composites with excellent visible-light photocatalytic activity. Mater Chem Phys 189:169–175. https://doi.org/10.1016/j.matchemphys.2016.12.028

Di TM, Zhu BC, Cheng B, Yu JG, Xu JS (2017) A direct Z-scheme g-C_3N_4/SnS_2 photocatalyst with superior visible-light CO_2 reduction performance. J Catal 352:532–541. https://doi.org/10.1016/j.jcat.2017.06.006

Ganjalinia A, Akbari S, Solouk A (2017) PLLA scaffolds surface-engineered via poly (propylene imine) dendrimers for improvement on its biocompatibility/controlled pH biodegradability. Appl Surf Sci 394:446–456. https://doi.org/10.1016/j.apsusc.2016.10.110

Hou Y, Wen Z, Cui S, Guo X, Chen J (2013) Constructing 2D porous graphitic C_3N_4 nanosheets/nitrogen-doped graphene/layered MoS_2 ternary nanojunction with enhanced photoelectrochemical activity. Adv Mater 25(43):6291–6297. https://doi.org/10.1002/adma.201303116

Ivanova I, Mendive CB, Bahnemann D (2016) The role of nanoparticulate agglomerates in TiO_2 photocatalysis: degradation of oxalic acid. J Nanopart Res 18(7):187–200. https://doi.org/10.1007/s11051-016-3495-x

Li G, Su R, Rao J, Wu J, Rudolf P, Blake G, Groot R, Besenbacher F, Palstra T (2016) Band gap narrowing of SnS_2 superstructures with improved hydrogen production. J Mater Chem A 4(1):209–216. https://doi.org/10.1039/C5TA07283B

Li X, Zhu J, Li H (2012) Comparative study on the mechanism in photocatalytic degradation of different-type organic dyes on SnS_2 and CdS. Appl Catal B: Environ 123–124:174–181

Liu G, Zhao G, Zhou W, Liu Y, Pang H, Zhang H, Hao D, Meng X, Li P, Kako T, Ye J (2016) In situ bond modulation of graphitic carbon nitride to construct p-n homojunctions for enhanced photocatalytic hydrogen production. Adv Funct Mater 26(37):6822–6829. https://doi.org/10.1002/adfm.201602779

Ma YN, Liu EZ, Hu XY, Tang CN, Wan J, Li J, Fan J (2015) A simple process to prepare few-layer g-C_3N_4 nanosheets with enhanced photocatalytic activities. Appl Surf Sci 358:246–251. https://doi.org/10.1016/j.apsusc.2015.08.174

Marien C, Cottineau T, Robert D, Drogui P (2016) TiO_2 nanotube arrays: influence of tube length on the photocatalytic degradation of Paraquat. Appl Catal B Environ 194:1–6. https://doi.org/10.1016/j.apcatb.2016.04.040

Miao H, Zhang G, Hu XY, Mu JL, Han T, Fan J, Zhu C, Song L, Bai JT, Hou X (2017) A novel strategy to prepare 2D g-C_3N_4 nanosheets and their photoelectrochemical properties. J Alloys Compd 690:669–676. https://doi.org/10.1016/j.jallcom.2016.08.184

Mu JL, Miao H, Liu EZ, Chen LD, Feng J, Han TX, Gao Y, Fan J, Hu XY (2017) Using Al_2O_3 defect levels to enhance the photoelectrocatalytic activity of SnS_2 nanosheets. Ceram Int 43(6):4992–5001. https://doi.org/10.1016/j.ceramint.2017.01.006

Pu CC, Wan J, Liu EZ, Yin YC, Li J, Ma YN, Fan J, Hu XY (2017) Two-dimensional porous architecture of protonated GCN and reduced graphene oxide via electrostatic self-assembly strategy for high photocatalytic hydrogen evolution under visible light. App Surf Sci 399:139–150. https://doi.org/10.1016/j.apsusc.2016.12.014

Ramadan W, Shaikh PA, Ebrahim S, Ramadan A, Hannoyer B, Jouen S, Sauvage X, Ogale S (2013) Highly efficient photocatalysis by $BiFeO_3$/$\alpha(\gamma)$-Fe_2O_3 ferromagnetic nano p/n junctions formed by dopant-induced phase separation. J Nanopart Res 15(8):1848–1858. https://doi.org/10.1007/s11051-013-1848-2

Ren Y, Lv W, Wen F, Xiang J, Liu Z (2016) Microwave synthesis of SnS_2 nanoflakes anchored graphene foam for flexible lithium-ion battery anodes with long cycling life. Mater Lett 174:24–27. https://doi.org/10.1016/j.matlet.2016.03.075

Shao D, Sun H, Gao J, Xin G, Aguilar M, Yao T, Koratkar N, Lian J, Sawyer S (2014) Flexible, thorn-like ZnO-multiwalled carbon nanotube hybrid paper for efficient ultraviolet sensing and photocatalyst applications. Nano 6:13630–13636

Sun M, Yan Q, Yan T, Li MM, Wei D, Wang ZP, Wei Q, Du B (2014) Facile fabrication of 3D flower-like heterostructured g-C_3N_4/SnS_2 composite with efficient photocatalytic activity under visible light. RSC Adv 4(59):31019–31027. https://doi.org/10.1039/C4RA03843F

Wang X, Maeda K, Chen X, Takanabe K, Domen K, Hou Y, Fu X, Antonietti M (2009) Polymer semiconductors for artificial photosynthesis: hydrogen evolution by mesoporous graphitic carbon nitride with visible light. J Am Chem Soc 131(5):1680–1861. https://doi.org/10.1021/ja809307s

Wang Y, Wang X, Antonietti M (2012) Polymeric graphitic carbon nitride as a heterogeneous organocatalyst: from photochemistry to multipurpose catalysis to sustainable chemistry. Angew Chem Int Ed 51(1):68–89. https://doi.org/10.1002/anie.201101182

Wu XF, Zhao ZH, Sun Y, Li H, Zhang CX, Wang YJ, Liu Y, Wang YD, Yang XY, Gong XD (2017) Preparation and characterization of Ag_2CrO_4/few layer boron nitride hybrids for visible-light-driven photocatalysis. J Nanopart Res 19(6):193–201. https://doi.org/10.1007/s11051-017-3892-9

Ye L, Liu J, Jiang Z, Peng T, Zan L (2013) Facets coupling of BiOBr-g-C_3N_4 composite photocatalyst for enhanced visible-light-driven photocatalytic activity. Appl Catal B: Environ 142–143:1–7

Yuan W, Zheng Y, Lu S, Xia T, Che Y, Chen J (2015) Visible-light-responsive TiO_2-coated ZnO: I nanorod array films with enhanced photoelectrochemical and photocatalytic performance. ACS Appl Mater Interfaces 7:6093–6101

Zhang G, Du X, Wang Y, Wang H, Wang W, Fu Z (2017) Controllable synthesis of SnS_2 nanostructures with high adsorption and photocatalytic activities. Mater Sci Semicond Process 64:77–84. https://doi.org/10.1016/j.mssp.2017.03.010

Zhang Y, Du Z, Li S, Zhang M (2010) Novel synthesis and high visible light photocatalytic activity of SnS_2 nanoflakes from $SnCl_2{\cdot}2H_2O$ and S powders. Appl Catal B Environ 95(1-2):153–159. https://doi.org/10.1016/j.apcatb.2009.12.022

Zhang Z, Huang J, Zhang M, Yuan Q, Dong B (2015a) Ultrathin hexagonal SnS_2 nanosheets coupled with g-C_3N_4 nanosheets as 2D/2D heterojunction photocatalysts toward high photocatalytic activity. Appl Catal B Environ 163:298–305. https://doi.org/10.1016/j.apcatb.2014.08.013

Zhang Y, Zhu P, Huang L, Xie J, Zhang S, Cao G, Zhao X (2015b) Few-layered SnS_2 on few-layered reduced graphene oxide as Na-ion battery anode with ultralong cycle life and superior rate capability. Adv Funct Mater 25(3):481–489. https://doi.org/10.1002/adfm.201402833

Zhao Z, Sun Y, Dong F (2014) Graphitic carbon nitride based nanocomposites: a review. Nano 7:15–37

Zhou L, Wang L, Lei J, Liu Y, Zhang J (2017) Fabrication of TiO_2/Co-g-C_3N_4 heterojunction catalyst and its photocatalytic performance. Catal Commun 89:125–128. https://doi.org/10.1016/j.catcom.2016.09.022